Raman Spectral Band Oscillations in Large Graphene Bubbles

Yuan Huang,[1,†] Xiao Wang,[1,†] Xu Zhang,[1] Xianjue Chen,[1] Baowen Li,[1] Bin Wang,[1] Ming Huang,[1,3] Chongyang Zhu,[1] Xuewei Zhang,[1,5] Wolfgang S. Bacsa,[4] Feng Ding,[1,3] and Rodney S. Ruoff[1,2,3,*]

[1]*Center for Multidimensional Carbon Materials (CMCM), Institute for Basic Science (IBS), Ulsan 44919, Republic of Korea*
[2]*Department of Chemistry, Ulsan National Institute of Science and Technology, Ulsan 44919, Republic of Korea*
[3]*School of Materials Science and Engineering, Ulsan National Institute of Science and Technology, Ulsan 44919, Republic of Korea*
[4]*CEMES-CNRS and University of Toulouse, 29 rue Jeanne Marvig, 31055 Toulouse, France*
[5]*Institute of Applied Mechanics and Key Laboratory of Soft Machines and Smart Devices of Zhejiang Province, Zhejiang University, Hangzhou 310012, People's Republic of China*

(Received 16 July 2017; revised manuscript received 21 December 2017; published 3 May 2018)

Raman spectra of large graphene bubbles showed size-dependent oscillations in spectral intensity and frequency, which originate from optical standing waves formed in the vicinity of the graphene surface. At a high laser power, local heating can lead to oscillations in the Raman frequency and also create a temperature gradient in the bubble. Based on Raman data, the temperature distribution within the graphene bubble was calculated, and it is shown that the heating effect of the laser is reduced when moving from the center of a bubble to its edge. By studying graphene bubbles, both the thermal conductivity and chemical reactivity of graphene were assessed. When exposed to hydrogen plasma, areas with bubbles are found to be more reactive than flat graphene.

DOI: 10.1103/PhysRevLett.120.186104

The electronic and mechanical properties of graphene can be tuned by reducing the lateral size, applying strain, or introducing curvature [1–3]. Because of the impermeability, exceptional flexibility, and excellent mechanical strength of the graphene sheet, bubbles can be formed on graphene [4–7]. Theoretical studies have shown that the radius and height of a bubble are determined by the energy balance between the strain energy of graphene, the potential energy of the gas inside the bubble, and the interfacial energy of the graphene layer with the substrate [8]. Thus, by measuring the bubble size, intrinsic properties such as the adhesion energy of graphene to the substrate can be determined [9], and this method can be extended to other 2D materials [10,11].

Raman spectroscopy is a versatile tool to identify the number of graphene layers, stacking and defect types, as well as strain [12–15]. In graphene, both the G and 2D bands are sensitive to strain; this strain dependence has been used to study the properties of graphene under uniaxial or biaxial stress [16–20]. Because of static effects on bond lengths and nonadiabatic electron-phonon coupling [21], both bands are also affected by doping, achieved either by applying an electrical field [22,23] or by chemical substitution [24–26]. Raman spectroscopy has also been used to investigate the biaxial strain distribution in graphene [15,16]. Thus, Raman spectroscopy of graphene bubbles can provide valuable information on the physical properties as well as on the chemical reactivity of graphene.

Graphene flakes were prepared by mechanical exfoliation from natural graphite and transferred onto a SiO_2/Si wafer (Fig. S1) [27,28]. A schematic of the preparation procedure is shown in Fig. 1(a). The formation of bubbles is due to the presence of adsorbed molecules on the polar SiO_2 surface that evaporate when heated, forming graphene bubbles [Fig. 1(a)]. Figure 1(b) shows the optical microscopy image of a circular graphene bubble where Newton rings caused by optical interference are clearly seen [7]. More detailed discussions about the sample preparation are presented in Supplemental Material [29].

Figure S2(a) shows the AFM image of a circular bubble on the graphene surface. The radius R of this bubble is 4.7 μm, and the maximum height h_{max} is 0.5 μm [Fig. S2(b) [29]], yielding an aspect ratio of $h_{max}/R \approx 11\%$, which is similar to that previously measured for graphene bubbles on a SiO_2/Si substrate (11%) [7]. More AFM images of graphene bubbles are shown in Fig. S3 [29]. Figure S2(c) shows Raman spectra measured on a graphene flake with bubbles. The four spectra shown in Fig. S2(c) were collected at different locations in the sample numbered 1–4 (Fig. S4 [29]). For regions 1 (2)

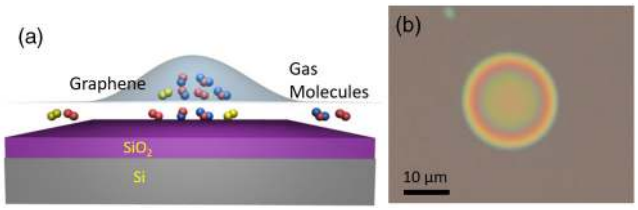

FIG. 1. (a) Schematic of a graphene bubble and trapped molecules between the SiO_2 surface and graphene. (b) Optical microscopy image of a graphene bubble (size 20 μm) on a 100 nm SiO_2/Si substrate showing Newton rings.

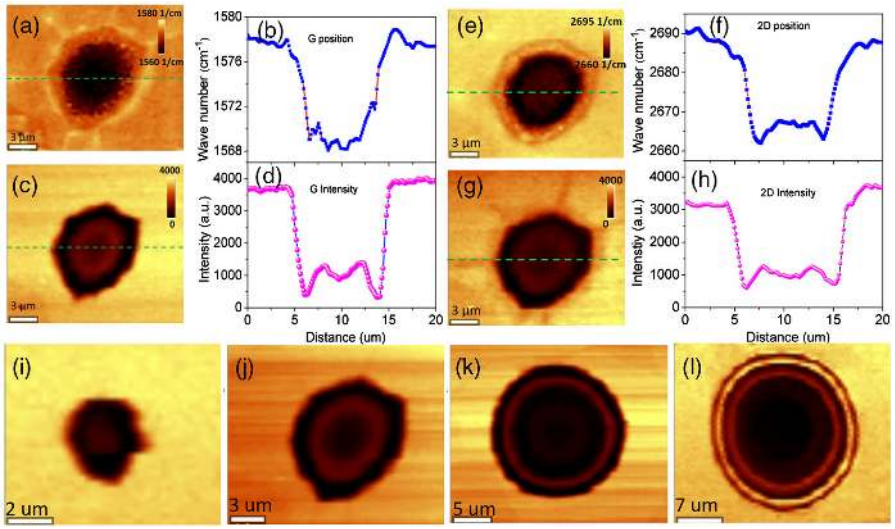

FIG. 2. Raman maps of the G peak position (a),(b) and intensity (c),(d) and the 2D band position (e),(f) and intensity (g),(h) for one graphene bubble. (i)–(l) Raman images (G band intensity) of graphene bubbles of different sizes.

corresponding to flat graphene on SiO_2, the G and 2D bands are located at 1576 (1574) and 2680 (2683) cm^{-1}, respectively. The values on flat graphene are close to reported values for exfoliated graphene except for a slight down-shift [37]. In contrast, Raman spectra taken on graphene bubbles (regions 3 and 4) are clearly down-shifted, similar to results reported by Zabel *et al.* [20]. The G peak shifts to 1558 cm^{-1}, and the 2D peak shifts to 2630 cm^{-1} for region 3.

While both G and 2D bands are sensitive to strain and doping [20], the influence of the two effects is different for the two modes. In the presence of compressive or tensile strain, a relatively large ratio of $\Delta\omega_{2D}/\Delta\omega_G$ in the range 2.02–2.44 is observed for graphene [15,19], where $\Delta\omega$ is the shift of the Raman peak with respect to the peak position measured on strain-free and undoped graphene. Hole doping induced by electrical field gating leads to quasilinearity ($\Delta\omega_{2D}/\Delta\omega_G = 0.75$) between ω_{2D} and ω_G [15], whereas for electron doping, this ratio becomes more nonlinear for higher doping levels [38]. Graphene as a suspended membrane can be charge-neutral (undoped) and also strain free, and, therefore, we use Raman band positions of what has been referred to as "freestanding" graphene as a reference, which is given in Fig. S5 [29]. The frequency shifts of the G and 2D modes ($\Delta\omega_G$ and $\Delta\omega_{2D}$) calculated with respect to these values are shown in Fig. S2 (d). The frequency shift ratio $\Delta\omega_{2D}/\Delta\omega_G$ is around 2.42 for the ten different bubbles. This ratio is consistent with the value reported in previous Raman studies on mechanically exfoliated undoped graphene samples, which were only mechanically strained [15,20,39]. Therefore, we can conclude that the peak shift of both the G and 2D bands shown in Fig. S2(c) is only due to strain.

Figures 2(a) and 2(c) show the peak position and intensity maps of the G mode on a 10 μm size graphene bubble. The G band frequency is lower at the center of the bubble and increases towards the edge. A similar behavior in frequency shift is observed for the 2D band shown in Figs. 2(e) and 2(g). The variations in G band positions are shown in Fig. 2(b) with the lowest G band frequency (1568 cm^{-1}) at the center of the bubble and the highest frequency (1579 cm^{-1}) on the flat area near the edges. Thus, it appears that the G band position shows oscillations and its intensity oscillates in a similar way [Fig. 2(c)]. The lowest intensity is not at the center of the bubble but around the edge, as seen in the cross-section image in Fig. 3(d). Figures 2(e)–2(h) show the Raman intensity and spectral position for the 2D band, where the variations are similar to those observed for the G band.

To better understand the oscillations in Raman intensity and spectral position, bubbles with different sizes were studied. Figures 2(i)–2(l) show the Raman G band maps of four bubbles with different diameters. In Fig. 2(i), the Raman intensity first decreases and then increases slightly at the center of the bubble (3.2 μm). In Fig. 2(j), the bright part around the center forms a ring around the larger bubble (10 μm). With increasing bubble size, both the number of rings and the fringe contrast increase [Figs. 2(k) and 2(l)]. Since the pressure inside a bubble is constant for a specific bubble [8,20,30,31], the strain at the bubble wall should also be nearly constant and, hence, the Raman peak position should not oscillate, which is contradictory to our observation. We note that, in larger bubbles, the focal spot of the laser is not anymore in focus due to the finite height of the bubble. This has the effect of reducing the detected G band intensity signal in the center [40].

Figure 3(a) shows a map of the G band spectral position for a large graphene bubble. Four rings can be clearly seen in the image corresponding to Raman shifts of the G band oscillating between 1550 and 1580 cm^{-1}. The G band

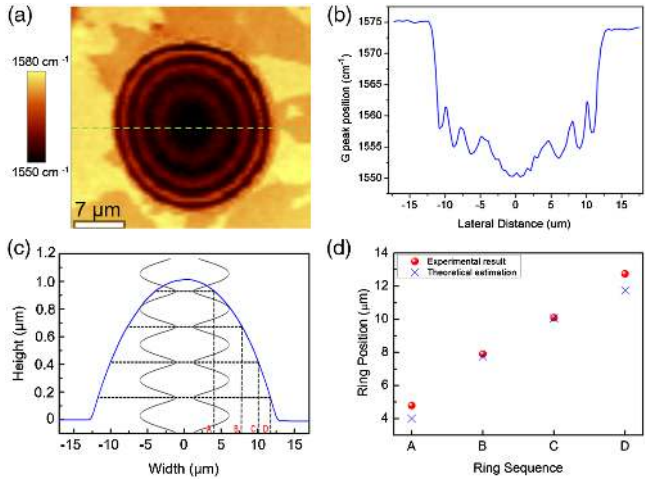

FIG. 3. The oscillation of the G band on a graphene bubble. (a) Raman map of the G band position of a bilayer graphene bubble. (b) G band line profile across the graphene bubble with an oscillation of the G band position. (c) Schematic of a standing wave showing intensity maxima. The radial positions with minimum amplitude are denoted as A, B, C, and D, which correspond to the bright rings in (a). (d) The experimental result and theoretical estimation of the positions of the bright rings.

position across the bubble profile is plotted in Fig. 3(b). The same bubble was imaged with AFM (bubble size, 25.5 μm; bubble height, 1.02 μm) and from the bubble profile [Fig. 3(c)], a strain of 0.37% is deduced. If we use the relation $(\partial\omega_G)/\partial\varepsilon = -25\ \mathrm{cm}^{-1}/\%$ [15,39], where ω is the Raman frequency and ε is the percent strain on graphene, the strain-induced Raman shift of the G band can be calculated to be 9.2 cm^{-1}. However, the total Raman shift of the G band at the bubble center is 30.2 cm^{-1} with respect to the G band position of freestanding graphene. The measured spectral shifts are thus substantially larger than what would be expected from only strain-induced effects.

We believe that the intensity oscillations of the Raman lines can be attributed to optical standing waves [41,42]. We note that Raman intensity variations as a function of the substrate and number of graphene layers have been observed earlier [42]. When a graphene bubble on a Si substrate is irradiated by laser light, ~40% of the laser will be reflected at the SiO_2/Si interface [43,44]. Standing waves will be formed by the interference of incident and reflected beams [Fig. 3(c)] generating interference maxima at certain distances from the graphene-substrate interface, where the distance between two maxima is $\lambda/2$ (more details in Supplemental Material [29]). The formation of optical standing waves near the substrate implies that the temperature of the bubble is highest at the point where the standing wave has an intensity maximum, which in turn implies different intensities of the optical field at different heights from the surface, thereby causing Raman G and 2D band intensities to oscillate. This phenomenon can be directly demonstrated by mapping the Raman G band for a bubble with a height of 1.02 μm, where four rings due to standing waves are observed [Fig. 3(a)]. Figure 3(d) compares the experimentally determined fringe radius with the calculated positions of the interference minima on the bubble; the obtained data show excellent agreement.

We verified that the heating-induced down-shifts of the Raman bands disappear if the laser power is reduced [Figs. S8(a) and 8(b) [29]]. Furthermore, we found that a prolonged (6 h) measurement on the same bubble can break the bubble and reduce its size (Fig. S6 [29]). We noted that extended exposure to laser illumination also had the effect to induce a Raman D band due to the formation of defects (Fig. S7 [29]). We also measured Raman spectra of bilayer graphene flakes for both suspended graphene and graphene flakes on the SiO_2/Si substrate [Figs. S8(c) and 8(d) [29]]. Both the G and 2D bands shift to a lower wave number as the laser power is increased from 1 to 21 mW.

Since the measured frequency shifts of the 2D and G bands depend on the temperature and the 2D band is more sensitive to temperature change [45], we chose the 2D band to estimate the thermal conductivity of the bubble wall. Taking the 2D band temperature coefficient of bilayer graphene from the literature [46], we estimate the average temperature at the laser spot according to the equation

$$\bar{T} = 300 + \frac{47.6}{0.034} = 1700\ \mathrm{K}. \tag{1}$$

Note that the value of the 2D band shift is derived from the difference between 2D band frequencies at the bubble center (2630.0 cm^{-1}) and at the bubble edge (2677.6 cm^{-1}). Applying the Fourier law and taking energy conservation into account, we can solve the temperature distribution equation as a function of the radial distance from the center of the graphene bubble r, assuming that the laser spot is at the center:

$$T(r) = \begin{cases} -\frac{P_0\alpha(r^2-r_0^2)}{4K\pi d r_0^2} + 1600 (r \le r_0), \\ -\frac{P_0\alpha}{2K\pi d}\ln\frac{r}{r_1} + 300 (r > r_0). \end{cases} \tag{2}$$

Here, r_0 is the radius of the laser spot, P_0 is the laser power (set as 20 mW), α is the absorbance of the graphene bubble (8.1% for bilayer graphene), and d is the thickness of bilayer graphene (6.7 Å) [36]. We can then calculate the thermal conductivity of the graphene bubble κ to be 958.9 $\mathrm{W/(m\,K)}$, which is in close agreement with previously reported values for bilayer graphene [1020 $\pm$ 120 $\mathrm{W/(m\,K)}$] determined by an optothermal Raman technique [46].

Based on the calculated thermal conductivity, we can plot the temperature distribution within the graphene bubble. Figure 4(a) shows the temperature distribution when the laser spot is at the center of the bubble, showing that the temperature decreases from the center to the edge [Figs. 4(a)–4(e)]. The temperature difference between the center and the edge of the laser spot is constant (200 K, Fig. S11 [29]), and that between the bubble edge and the

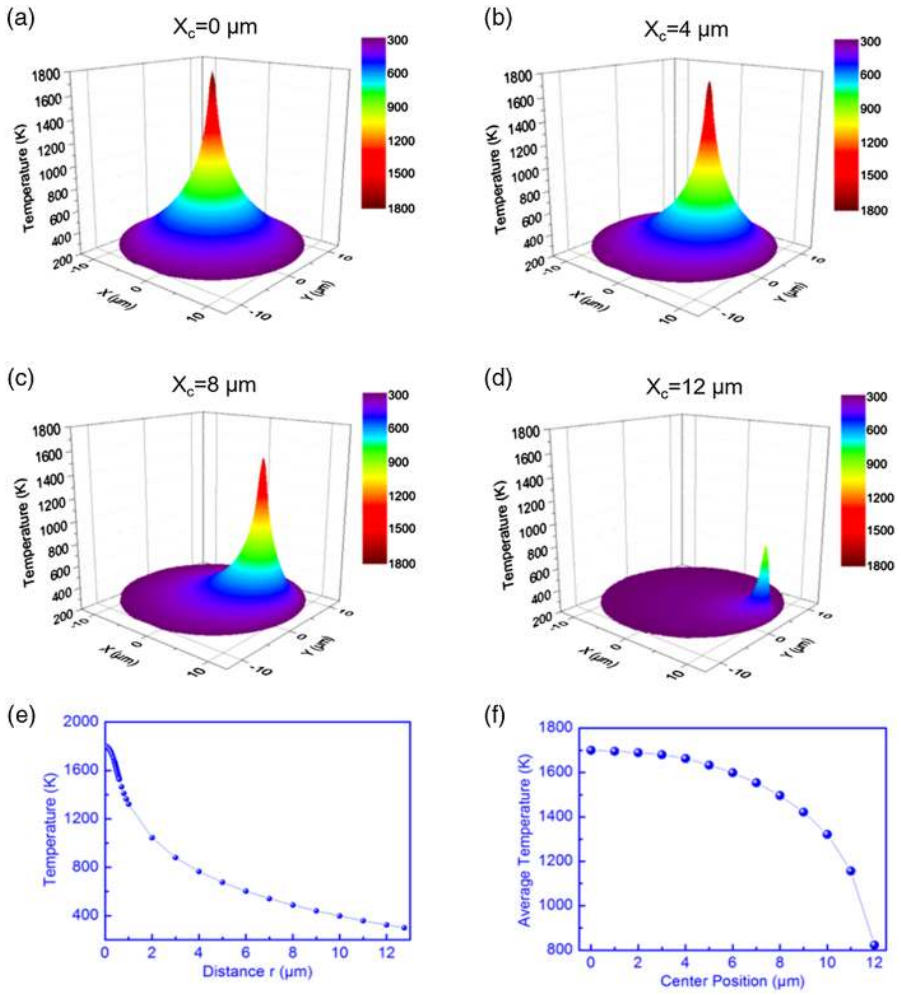

FIG. 4. Temperature distribution on a graphene bubble as a function of the laser spot position. (a)–(d) Temperature distribution on a graphene bubble at different laser spot positions; X_c is the distance between the center of the laser spot and the center of the bubble. (e) Temperature distribution on the graphene bubble when the laser focus is located at the center of the bubble. (f) Average temperature at the position of the laser spot for different locations on the graphene bubble.

edge of the laser spot is proportional to $\ln(r_1/r_0)$. For a larger bubble, the temperature difference between the center and edge will be higher (Fig. S12 [29]). As the laser spot moves away from the center to the edge of the bubble [Figs. 4(b)–4(d)], the temperature distribution is different from that shown in Fig. 4(a). The average temperature within the laser spot decreases from 1700 to 800 K when the spot moves from $X_c = 0$ to $X_c = 12$ μm, implying a drastic reduction of the heating effect [Fig. 4(f)]. A similar tendency is observed for the maximum temperature within the bubble (Fig. S14). Since the G band wave number correlates negatively to the temperature, it should also increase when the laser spot is moved from the center to the edge of the bubble. Our experiments have shown that this is indeed the case [Fig. 3(b)].

The increased strain in a graphene bubble can influence its reactivity. Anisotropic etching is widely used to study the properties of 2D materials and design special structures [47,48] such as graphene nanoribbons, hexagonal pits, and triangular flakes [47]. We have tested the reactivity of the graphene bubbles by exposing them to hydrogen plasma; the experimental protocol and AFM images of bubbles before and after plasma treatment are given in Supplemental Material (Fig. S9 [29]). We find that carbon atoms are more chemically active in areas with larger strain, especially in triangular bubbles, which means that such bubbles could be potentially useful to generate functional graphene surfaces.

In summary, we find that optical standing waves oriented parallel to the substrate surface induce oscillations of intensity and frequency of Raman bands in large graphene bubbles, leading to the nonuniform heating of the bubble. Theoretical modeling has shown that the temperature distribution in a graphene bubble depends on the location of the laser spot on the graphene bubble, from which the thermal conductivity of graphene was estimated. Thus, studying graphene bubbles can lead to a new understanding of the physical and chemical properties of graphene.

This work was supported by the Institute for Basic Science (IBS-R019-D1). W. S. B. was partly supported by the University of Toulouse and NEXT (ANR-10-LABEX-0037). We thank Dr. Revathi R. Bacsa for discussion and valuable comments.

*rsruoff@ibs.re.kr, ruofflab@gmail.com
†Y. H. and X. W. contributed equally to this work.

[1] M. P. Lopez-Sancho and M. C. Munoz, Phys. Rev. B **83**, 075406 (2011).
[2] D. Huertas-Hernando, F. Guinea, and A. Brataas, Phys. Rev. B **74**, 155426 (2006).
[3] J. M. Cai *et al.*, Nat. Nanotechnol. **9**, 896 (2014).
[4] J. S. Bunch, S. S. Verbridge, J. S. Alden, A. M. van der Zande, J. M. Parpia, H. G. Craighead, and P. L. McEuen, Nano Lett. **8**, 2458 (2008).
[5] N. G. Boddeti, S. P. Koenig, R. Long, J. L. Xiao, J. S. Bunch, and M. L. Dunn, J. Appl. Mech. **80**, 040909 (2013).
[6] N. G. Boddeti, X. Liu, R. Long, J. Xiao, J. S. Bunch, and M. L. Dunn, Nano Lett. **13**, 6216 (2013).
[7] T. Georgiou, L. Britnell, P. Blake, R. V. Gorbachev, A. Gholinia, A. K. Geim, C. Casiraghi, and K. S. Novoselov, Appl. Phys. Lett. **99**, 093103 (2011).
[8] K. M. Yue, W. Gao, R. Huang, and K. M. Liechti, J. Appl. Phys. **112**, 083512 (2012).
[9] S. P. Koenig, N. G. Boddeti, M. L. Dunn, and J. S. Bunch, Nat. Nanotechnol. **6**, 543 (2011).
[10] D. Lloyd, X. H. Liu, N. Boddeti, L. Cantley, R. Long, M. L. Dunn, and J. S. Bunch, Nano Lett. **17**, 5329 (2017).
[11] D. Lloyd, X. H. Liu, J. W. Christopher, L. Cantley, A. Wadehra, B. L. Kim, B. B. Goldberg, A. K. Swan, and J. S. Bunch, Nano Lett. **16**, 5836 (2016).
[12] S. W. Schmucker, C. D. Cress, J. C. Culbertson, J. W. Beeman, O. D. Dubon, and J. T. Robinson, Carbon **93**, 250 (2015).
[13] S. Kim and S. Ryu, Carbon **100**, 283 (2016).
[14] J. B. Wu, Z. X. Hu, X. Zhang, W. P. Han, Y. Lu, W. Shi, X. F. Qiao, M. Ijias, S. Milana, W. Ji, A. C. Ferrari, and P. T. Tan, ACS Nano **9**, 7440 (2015).
[15] J. E. Lee, G. Ahn, J. Shim, Y. S. Lee, and S. Ryu, Nat. Commun. **3**, 1024 (2012).
[16] F. Ding, H. X. Ji, Y. H. Chen, A. Herklotz, K. Dorr, Y. F. Mei, A. Rastelli, and O. G. Schmidt, Nano Lett. **10**, 3453 (2010).
[17] C. Metzger, S. Remi, M. Liu, S. V. Kusminskiy, A. H. Castro Neto, A. K. Swan, and B. B. Goldberg, Nano Lett. **10**, 6 (2010).
[18] M. Y. Huang, H. G. Yan, C. Y. Chen, D. H. Song, T. F. Heinz, and J. Hone, Proc. Natl. Acad. Sci. U.S.A. **106**, 7304 (2009).
[19] D. Yoon, Y. W. Son, and H. Cheong, Phys. Rev. Lett. **106**, 155502 (2011).
[20] J. Zabel, R. R. Nair, A. Ott, T. Georgiou, A. K. Geim, K. S. Novoselov, and C. Casiraghi, Nano Lett. **12**, 617 (2012).
[21] M. Lazzeri and F. Mauri, Phys. Rev. Lett. **97**, 266407 (2006).
[22] J. Yan, Y. Zhang, P. Kim, and A. Pinczuk, Phys. Rev. Lett. **98**, 166802 (2007).
[23] S. Pisana, M. Lazzeri, C. Casiraghi, K. S. Novoselov, A. K. Geim, A. C. Ferrari, and F. Mauri, Nat. Mater. **6**, 198 (2007).
[24] S. Ryu, L. Liu, S. Berciaud, Y. J. Yu, H. T. Liu, P. Kim, G. W. Flynn, and L. E. Brus, Nano Lett. **10**, 4944 (2010).
[25] L. Liu, S. M. Ryu, M. R. Tomasik, E. Stolyarova, N. Jung, M. S. Hybertsen, M. L. Steigerwald, L. E. Brus, and G. W. Flynn, Nano Lett. **8**, 1965 (2008).
[26] S. Berciaud, S. Ryu, L. E. Brus, and T. F. Heinz, Nano Lett. **9**, 346 (2009).
[27] K. S. Novoselov, A. K. Geim, S. V. Morozov, D. Jiang, Y. Zhang, S. V. Dubonos, I. V. Grigorieva, and A. A. Firsov, Science **306**, 666 (2004).
[28] Y. Huang, E. Sutter, N. N. Shi, J. B. Zheng, T. Z. Yang, D. Englund, H. J. Gao, and P. Sutter, ACS Nano **9**, 10612 (2015).
[29] See Supplemental Material at http://link.aps.org/supplemental/10.1103/PhysRevLett.120.186104, which includes Refs. [30–36], for sample preparation, optical microscope and AFM characterization, calculation details of pressure within the bubble, Raman measurement, and a theoretical model for temperature distribution and thermal conductivity.
[30] C. Lee, X. D. Wei, J. W. Kysar, and J. Hone, Science **321**, 385 (2008).
[31] K. N. Kudin, G. E. Scuseria, and B. I. Yakobson, Phys. Rev. B **64**, 235406 (2001).
[32] H. Hencky, Z. Math. Phys. **63**, 311 (1915).
[33] J. G. Williams, Int. J. Fract. **87**, 265 (1997).
[34] A. L. Kitt, Z. N. Qi, S. Remi, H. S. Park, A. K. Swan, and B. B. Goldberg, Nano Lett. **13**, 2605 (2013).
[35] Z. Z. Sun, Z. Yan, J. Yao, E. Beitler, Y. Zhu, and J. M. Tour, Nature (London) **468**, 549 (2010).
[36] R. R. Nair, P. Blake, A. N. Grigorenko, K. S. Novoselov, T. J. Booth, T. Stauber, N. M. R. Peres, and A. K. Geim, Science **320**, 1308 (2008).
[37] A. C. Ferrari, J. C. Meyer, V. Scardaci, C. Casiraghi, M. Lazzeri, F. Mauri, S. Piscanec, D. Jiang, K. S. Novoselov, S. Roth, and A. K. Geim, Phys. Rev. Lett. **97**, 187401 (2006).
[38] A. Das, B. Chakraborty, S. Piscanec, S. Pisana, A. K. Sood, and A. C. Ferrari, Phys. Rev. B **79**, 155417 (2009).
[39] T. M. G. Mohiuddin, A. Lombardo, R. R. Nair, A. Bonetti, G. Savini, R. Jalil, N. Bonini, D. M. Basko, C. Galiotis, N. Marzari, K. S. Novoselov, A. K. Geim, and A. C. Ferrari, Phys. Rev. B **79**, 205433 (2009).
[40] W. S. Bacsa, E. Pavlenko, and V. Tishkova, Nanomater. Nanotechnol. **3**, 22 (2013).
[41] W. Bacsa and J. Lannin, Appl. Phys. Lett. **61**, 19 (1992).
[42] P. Klar, E. Lidorikis, A. Eckmann, I. A. Verzhbitskiy, A. C. Ferrari, and C. Casiraghi, Phys. Rev. B **87**, 205435 (2013).
[43] S. A. A. Oloomi, A. Saboonchi, and A. Sedaghat, Int. J. Phys. Sci. **5**, 465 (2010).
[44] A. Convertino, M. Cuscuna, and F. Martelli, Nanotechnology **21**, 355701 (2010).
[45] S. S. Chen *et al.*, ACS Nano **5**, 321 (2011).
[46] H. Y. Li, H. Ying, X. P. Chen, D. L. Nika, A. I. Cocemasov, W. W. Cai, A. A. Balandin, and S. S. Chen, Nanoscale **6**, 13402 (2014).
[47] R. Yang, L. C. Zhang, Y. Wang, Z. W. Shi, D. X. Shi, H. J. Gao, E. G. Wang, and G. Y. Zhang, Adv. Mater. **22**, 4014 (2010).
[48] Y. Huang, J. Wu, X. Xu, Y. Ho, G. Ni, Q. Zou, G. K. W. Koon, W. Zhao, A. H. C. Neto, G. Eda, C. Shen, and B. Özyilmaz, Nano Res. **6**, 200 (2013).